


# Thermal transport and energy dissipation in two-dimensional Bi<sub>2</sub>O<sub>2</sub>Se

Cite as: Appl. Phys. Lett. **115**, 193103 (2019); <https://doi.org/10.1063/1.5123682>

Submitted: 10 August 2019 . Accepted: 20 October 2019 . Published Online: 05 November 2019

Fang Yang, Ridong Wang, Weiwei Zhao, Jie Jiang, Xin Wei, Ting Zheng, Yutian Yang, Xinwei Wang, Junpeng Lu , and Zhenhua Ni



View Online



Export Citation



CrossMark

## ARTICLES YOU MAY BE INTERESTED IN

[Hetero-integration of quasi two-dimensional PbZr<sub>0.2</sub>Ti<sub>0.8</sub>O<sub>3</sub> on AlGa<sub>N</sub>/Ga<sub>N</sub> HEMT and non-volatile modulation of two-dimensional electron gas](#)

Applied Physics Letters **115**, 193505 (2019); <https://doi.org/10.1063/1.5123192>

[Spatially resolved optical excitation of mechanical modes in graphene NEMS](#)

Applied Physics Letters **115**, 193102 (2019); <https://doi.org/10.1063/1.5111755>

[Plasma formation and relaxation dynamics in fused silica driven by femtosecond short-wavelength infrared laser pulses](#)

Applied Physics Letters **115**, 191903 (2019); <https://doi.org/10.1063/1.5117837>



**Measure Ready**  
**M91 FastHall™ Controller**

A revolutionary new instrument  
for complete Hall analysis

[See the video](#)

**Lake Shore**  
CRYOTRONICS

# Thermal transport and energy dissipation in two-dimensional Bi<sub>2</sub>O<sub>2</sub>Se

Cite as: Appl. Phys. Lett. **115**, 193103 (2019); doi: [10.1063/1.5123682](https://doi.org/10.1063/1.5123682)

Submitted: 10 August 2019 · Accepted: 20 October 2019 ·

Published Online: 5 November 2019




View Online



Export Citation



CrossMark

Fang Yang,<sup>1,a)</sup> Ridong Wang,<sup>2,a)</sup> Weiwei Zhao,<sup>1</sup> Jie Jiang,<sup>1</sup> Xin Wei,<sup>1</sup> Ting Zheng,<sup>1</sup> Yutian Yang,<sup>1</sup> Xinwei Wang,<sup>2</sup> Junpeng Lu,<sup>1,b)</sup>  and Zhenhua Ni<sup>1,b)</sup>

## AFFILIATIONS

<sup>1</sup>School of Physics, Southeast University, Nanjing 211189, China

<sup>2</sup>Department of Mechanical Engineering, Iowa State University, 271 Applied Science Complex II, Ames, Iowa 50011, USA

<sup>a)</sup>Contributions: F. Yang and R. Wang contributed equally to this work.

<sup>b)</sup>Authors to whom correspondence should be addressed: [phyljlp@seu.edu.cn](mailto:phyljlp@seu.edu.cn) and [zhni@seu.edu.cn](mailto:zhni@seu.edu.cn)

## ABSTRACT

Thermal transport and energy dissipation are important for a material in both thermoelectric and electronic devices. Here, we investigate the lateral and interfacial thermal transport of two-dimensional (2D) Bi<sub>2</sub>O<sub>2</sub>Se by Raman spectroscopy. It is found that thin Bi<sub>2</sub>O<sub>2</sub>Se flakes have a low in-plane thermal conductivity while maintaining an appropriate interfacial thermal conductance. The in-plane thermal conductivity of Bi<sub>2</sub>O<sub>2</sub>Se decreases with decreasing thickness, to as low as  $0.92 \pm 0.18 \text{ W}\cdot\text{m}^{-1}\cdot\text{K}^{-1}$  at a thickness of  $\sim 8 \text{ nm}$ . Such a low thermal conductivity is derived from the low phonon group velocity, strong anharmonicity, and large surface scattering of acoustic phonons of the Bi<sub>2</sub>O<sub>2</sub>Se thin layer. Simultaneously, thinner Bi<sub>2</sub>O<sub>2</sub>Se presents a higher thermal dissipation to the substrate than the thicker counterparts in the device. The interfacial thermal conductance increases with decreasing thickness, and reaches  $\sim 21 \text{ MW}\cdot\text{m}^{-2}\cdot\text{K}^{-1}$  at  $\sim 8 \text{ nm}$ . These results provide critical information for the design of thermoelectric devices with high figures of merit and electronics with low-power consumption based on 2D materials.

Published under license by AIP Publishing. <https://doi.org/10.1063/1.5123682>

Thermal transport in two-dimensional (2D) materials has attracted extensive research interest because it is crucial in determining their potential applications in thermal management, nanoelectronics, and thermoelectric devices.<sup>1,2</sup> Some 2D materials are well-known for their high in-plane thermal conductivity. For example, the thermal conductivity of graphene is  $\sim 5300 \text{ W}\cdot\text{m}^{-1}\cdot\text{K}^{-1}$  because of the long phonon mean free path (MFP) and the high group velocities of acoustic phonons.<sup>2</sup> On the other hand, a low thermal conductivity is also of great importance as it can increase the thermoelectric figure of merit (ZT) and thereby improve the thermoelectric conversion efficiency.<sup>3</sup> Two-dimensional Pb<sub>2</sub>Se<sub>3</sub> and InSe flakes have been demonstrated to have a low in-plane thermal conductivity ( $1\text{--}3 \text{ W}\cdot\text{m}^{-1}\cdot\text{K}^{-1}$ ). These values are comparable to the thermal conductivity of bulk thermoelectric materials.<sup>4</sup> However, to realize the application of 2D materials in thermoelectrics, a lower thermal conductivity would provide a better device performance.<sup>3,5</sup> To achieve an ultralow thermal conductivity, materials are required to have a low phonon group velocity and strong anharmonicity. Recently, an emerging 2D semiconductor, Bi<sub>2</sub>O<sub>2</sub>Se, has attracted widespread attention because of its superior electrical transport properties.<sup>6</sup> Substitution of selenium atoms with oxygen

could eliminate the metal surface state of Bi<sub>2</sub>Se<sub>3</sub> and introduce a transformation from a topological insulator to a high mobility semiconductor. The opening of the bandgap could also give Bi<sub>2</sub>O<sub>2</sub>Se a larger Seebeck coefficient than Bi<sub>2</sub>Se<sub>3</sub>, which would make it a potential high-ZT thermoelectric material.

Herein, thermal transport behaviors including the in-plane and interfacial thermal conductance of 2D Bi<sub>2</sub>O<sub>2</sub>Se are measured by using micro-Raman spectroscopy as a non-contact technique.<sup>1</sup> We found the in-plane thermal conductivity of Bi<sub>2</sub>O<sub>2</sub>Se flakes decreases with decreasing thickness, exhibiting a low thermal conductivity of  $0.92 \pm 0.18 \text{ W}\cdot\text{m}^{-1}\cdot\text{K}^{-1}$  at a thickness of  $\sim 8 \text{ nm}$ . This is much lower than the in-plane thermal conductivity of common 2D materials such as MoS<sub>2</sub> and black phosphorus.<sup>7,8</sup> The low thermal conductivity of Bi<sub>2</sub>O<sub>2</sub>Se was expected by the theoretical calculation ( $0.66 \text{ W}\cdot\text{m}^{-1}\cdot\text{K}^{-1}$  for the monolayer)<sup>9</sup> and experimentally demonstrated by measuring the thermal conductivity of pressed powders ( $\sim 1.1 \text{ W}\cdot\text{m}^{-1}\cdot\text{K}^{-1}$ ).<sup>10,11</sup> However, the barriers between powder to powder would increase the resistance and affect the precision of the measurements. In our study, we employ individual Bi<sub>2</sub>O<sub>2</sub>Se flakes to carry out the measurements. The low thermal conductivity of the Bi<sub>2</sub>O<sub>2</sub>Se thin flake originates from

the low phonon group velocity, strong anharmonicity, and large surface scattering of acoustic phonons. Moreover, the interfacial thermal conductance of the  $\text{Bi}_2\text{O}_2\text{Se}$  and substrate ( $\text{SiO}_2/\text{Si}$ ) is also thickness dependent. Contrary to the in-plane thermal conductivity, 2D  $\text{Bi}_2\text{O}_2\text{Se}$  flakes have higher interfacial thermal conductance values than the bulk counterparts, which is due to the larger interface adhesion energy of thinner flakes.

As shown in Fig. 1(a), layered 2D  $\text{Bi}_2\text{O}_2\text{Se}$  exhibits a tetragonal structure and space group symmetry  $I4/mmm$  ( $a = b = 3.88 \text{ \AA}$ ,  $c = 12.16 \text{ \AA}$ ). The  $[\text{Se}]_n^{2n-}$  layers are sandwiched between strong covalently bonded oxide  $[\text{Bi}_2\text{O}_2]_n^{2n+}$  layers by a weak electrostatic interaction. Two-dimensional  $\text{Bi}_2\text{O}_2\text{Se}$  flakes with controlled thicknesses were synthesized on a mica surface by chemical vapor deposition (CVD) methods [Fig. 1(b)]. The detailed fabrication processes are described in the supplementary material. As shown in Fig. 1(c), the as-grown  $\text{Bi}_2\text{O}_2\text{Se}$  flakes have a square shape and exhibit a large domain size of  $10\text{--}20 \mu\text{m}$ . An AFM image [Fig. 1(d)] shows that the roughness of the surface of the as-grown flake is  $\sim 0.5 \text{ nm}$  and the thickness is  $\sim 6 \text{ nm}$ . Other  $\text{Bi}_2\text{O}_2\text{Se}$  flakes with different thicknesses ranging from  $8\text{--}40 \text{ nm}$  were synthesized and are displayed in Fig. S1(a)–S1(e). The  $\text{Bi}_2\text{O}_2\text{Se}$  flakes were transferred onto a  $300 \text{ nm SiO}_2/\text{Si}$  substrate or a regular Cu grid by using the PMMA-mediated method for further investigation [Fig. S2(a)]. Clear signals of Bi, Se, and O were detected by energy-dispersive X-ray spectroscopy (EDX). Quantitative analysis showed a 2:1 atomic ratio for the Bi and Se stoichiometry [Figs. 1(e) and S1(f)–S1(h)].

According to the group theory, there are four Raman modes expected for  $\text{Bi}_2\text{O}_2\text{Se}$ :  $E_g^1$ ,  $A_{1g}$ ,  $B_{1g}$ , and  $E_g^2$ .<sup>12</sup> Only the  $A_{1g}$  ( $\sim 157 \text{ cm}^{-1}$ ) mode is observed in our samples, because the  $B_{1g}$  and  $E_g^2$  peaks are too weak and the low frequency  $E_g^1$  mode is outside the detection range of our equipment [Fig. 1(f)]. This result is consistent with a previous report.<sup>12</sup> The Raman spectra of  $\text{Bi}_2\text{O}_2\text{Se}$  with the temperature ranging from  $50\text{--}300 \text{ K}$  are shown in Fig. 1(g), which shows

continuous redshifts with increasing temperature. The frequency of the Raman mode can be expressed as  $\omega(T) = \omega_0 + \chi \times T$ , where  $\omega_0$  is the frequency of  $A_{1g}$  at  $0 \text{ K}$  and  $\chi$  is the temperature coefficient. The extracted temperature coefficient for  $\sim 8 \text{ nm Bi}_2\text{O}_2\text{Se}$  is  $\chi = 0.0167 \text{ cm}^{-1}/\text{T}$ , which is slightly larger than the few-layer sample of  $\text{MoS}_2$  ( $0.0132 \text{ cm}^{-1}/\text{T}$  for the  $A_{1g}$  mode) and the  $\text{WS}_2$  monolayer ( $0.0149 \text{ cm}^{-1}/\text{T}$  for the  $A_{1g}$  mode) and the bulk  $\text{Bi}_2\text{O}_2\text{Se}$  ( $0.0125 \text{ cm}^{-1}/\text{T}$ ).<sup>7,13</sup> The large temperature coefficient of the  $A_{1g}$  mode arises from the anharmonicity in the interatomic potential energy caused by the phonon-phonon interactions. The  $A_{1g}$  mode in thinner  $\text{Bi}_2\text{O}_2\text{Se}$  has a stronger temperature response than in the thicker counterparts because it suffers less vibrational restriction from the weak interlayer interactions.<sup>14</sup> Figure 1(h) summarizes the Raman frequencies of four  $\text{Bi}_2\text{O}_2\text{Se}$  flakes with different thicknesses versus temperature. Since the shift of the Raman peak shows a good linear relationship with the change of temperature, it is valid to deduce the temperature of the samples based on the peak shift.

In the optothermal Raman measurements, a focused laser beam serves as a steady-state heat source to heat the sample suspended on a Cu grid [inset of Fig. 2(a)]. The in-plane thermal conductivity can then be deduced considering the temperature distribution determined by the power of the incident laser. With increasing laser power ( $p$ ), the increased temperature causes red shifts ( $\omega$ ) of the Raman peak [Fig. 2(a)]. Notably,  $\Delta\omega/\Delta p$  increases with decreasing thickness. For  $\sim 8 \text{ nm Bi}_2\text{O}_2\text{Se}$ , the  $A_{1g}$  Raman peak presents a significant shift of  $\sim 1.5 \text{ cm}^{-1}$  even at a relatively low laser power of  $\sim 37 \mu\text{W}$ . The  $\Delta\omega/\Delta p$  ratio is much higher than the other 2D materials, indicating a lower in-plane thermal conductivity.<sup>7</sup> For bulk  $\text{Bi}_2\text{O}_2\text{Se}$  ( $\sim 40 \text{ nm}$ ), the peak shift is  $\sim 1.5 \text{ cm}^{-1}$  when the laser power reaches  $\sim 110 \mu\text{W}$ , showing a higher in-plane thermal conductivity. According to the measured temperature coefficient  $\chi$ , the temperature distribution of the sample at a certain power can be calculated. The energy transport in the sample (at the steady-state heating condition) is governed by

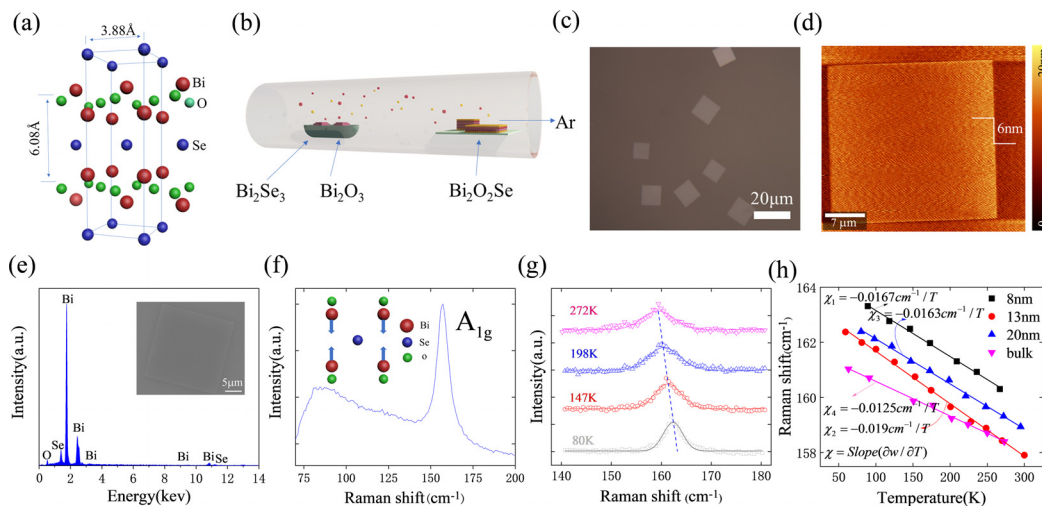


**FIG. 1.** CVD growth and characterization of  $\text{Bi}_2\text{O}_2\text{Se}$  flakes. (a) Crystal structure of  $\text{Bi}_2\text{O}_2\text{Se}$ . (b) Schematic illustration of a CVD system used in 2D  $\text{Bi}_2\text{O}_2\text{Se}$  synthesis. (c) Typical optical microscopy image of  $\text{Bi}_2\text{O}_2\text{Se}$  flakes grown on a mica substrate. (d) AFM image of a typical  $\text{Bi}_2\text{O}_2\text{Se}$  flake with a thickness of  $\sim 6 \text{ nm}$ . (e) EDX spectrum of a typical  $\text{Bi}_2\text{O}_2\text{Se}$  flake. The inset shows a scanning electron microscopy image. (f) Raman spectrum of a typical  $\text{Bi}_2\text{O}_2\text{Se}$  flake. The inset illustrates the  $A_{1g}$  vibration mode of. (g) Raman frequency evolution  $\text{Bi}_2\text{O}_2\text{Se}$  flake with a thickness of  $\sim 20 \text{ nm}$  at four different temperatures. (h) First-order temperature coefficient of  $\text{Bi}_2\text{O}_2\text{Se}$  flakes extracted from the shifts of  $A_{1g}$  modes. The experimental results are fitted using linear functions.

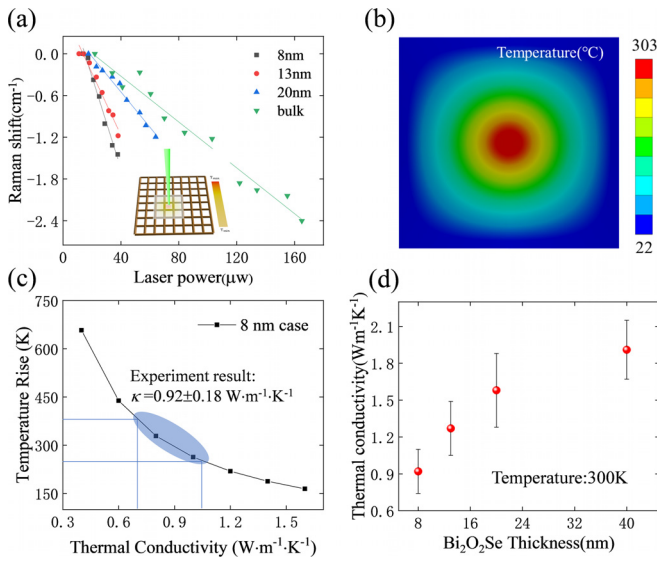


**FIG. 2.** In-plane thermal conductivity of  $\text{Bi}_2\text{O}_2\text{Se}$  flakes. (a) Power dependence of the  $A_{1g}$  peak frequencies of  $\text{Bi}_2\text{O}_2\text{Se}$  flakes with different thicknesses. (b) 3D numerical modeling of the heat conduction at the steady state. Temperature and Raman intensity distribution in the space domain are shown. (c) The average temperature rise of the  $\sim 8$  nm  $\text{Bi}_2\text{O}_2\text{Se}$  flake with increasing thermal conductivity at the steady state. (d) Extracted in-plane thermal conductivities of  $\text{Bi}_2\text{O}_2\text{Se}$  flakes with different thicknesses.

$$\kappa \nabla^2 \Delta T + I = 0, \quad (1)$$

where  $\Delta T$  (K) is the temperature rise.  $\kappa$  ( $\text{W}\cdot\text{m}^{-1}\cdot\text{K}^{-1}$ ) is the in-plane thermal conductivity.  $I$  is volumetric Gaussian beam heating

$$I(r, z) = \frac{I_0}{\tau_L} \exp\left(-\frac{r^2}{r_0^2}\right) \exp\left(-\frac{z}{\tau_L}\right), \quad (2)$$

where  $r$  is radial position from the grid center [Fig. S2(a)].  $\tau_L$  is the laser absorption depth. The measured absorptivity for  $\sim 8$  nm  $\text{Bi}_2\text{O}_2\text{Se}$  is  $\sim 14.0\%$  [Fig. S2(b)].  $I_0 = P/\pi r_0^2$  is the power density at the center of the laser spot.  $r_0$  ( $\mu\text{m}$ ) is the radius of the laser spot, which is obtained from fitting the experimental data with an error function. The details are shown in Figs. S2(c) and S3. As shown in Fig. 2(b), the temperature rise at the steady state is calculated via a 3D numerical modeling based on the finite volume method. The Raman intensity weighted average temperature rise over space ( $\Delta \bar{T}|_{\text{theoretical}}$ ) is obtained. This simulation process is performed for different  $\kappa$  values to determine the theoretical curve of  $\Delta \bar{T}$  against  $\kappa$ .<sup>15</sup> Figure 2(c) shows the temperature rise of  $\sim 8$  nm  $\text{Bi}_2\text{O}_2\text{Se}$  under the steady state heating in our model. The  $\partial p_{\text{absorb}}/\partial T$  for the  $\sim 8$  nm  $\text{Bi}_2\text{O}_2\text{Se}$  is around  $0.041 \mu\text{W}/\text{K}$ . When the absorption power of the sample reaches  $10 \mu\text{W}$ , the temperature rise is around  $300 \text{ K}$ . The  $\kappa$  of  $\text{Bi}_2\text{O}_2\text{Se}$  at the thickness of  $\sim 8$  nm is calculated to be  $0.92 \pm 0.18 \text{ W}\cdot\text{m}^{-1}\cdot\text{K}^{-1}$ . This value is much lower than the thermal conductivity of  $\text{Bi}_2\text{Te}_3$  ( $\sim 1.5 \text{ W}\cdot\text{m}^{-1}\cdot\text{K}^{-1}$ ), which is one of the most efficient thermoelectric materials.<sup>16</sup> The low in-plane thermal conductivity of 2D  $\text{Bi}_2\text{O}_2\text{Se}$  would originate from the low phonon velocity and strong anharmonicity. It should be noted that the thermal conductivity arises from both electrons and phonons. The contribution of electrons ( $\kappa_e = L\sigma T$ ) to thermal conductivity is

strongly dependent on the Lorenz number ( $L$ ) and electrical conductivity ( $\sigma$ ). Due to the relatively large resistivity ( $\rho > 10^{-5} \Omega\cdot\text{m}$ ) of a semiconductor, the contribution from electrons is negligible. The majority of the thermal conductivity is contributed by phonons, which is the lattice thermal conductivity ( $\kappa_L$ ), determined by<sup>17</sup>

$$\kappa_L = \frac{1}{3} c_v v_g^2 \tau, \quad (3)$$

where  $v_g$  is the group velocity,  $c_v$  is the specific heat, and  $\tau$  is the phonon relaxation time. The lattice is simplified to a model wherein balls are connected by springs. The atoms correspond to the balls with an average mass,  $M$ , and the restoring force is  $F$ . So, the phonon group velocity  $v_s$  depends on  $(F/M)^{1/2}$ . According to the crystal structure of  $\text{Bi}_2\text{O}_2\text{Se}$  [Fig. 1(a)], the Se square arrays are sandwiched between covalently bonded oxide layers ( $\text{Bi}_2\text{O}_2$ ). The radii of  $\text{Bi}^{3+}$  and  $\text{Se}^{2-}$  ions are  $1.03 \text{ \AA}$  and  $1.98 \text{ \AA}$ , respectively, while the distance between Bi and Se in  $\text{Bi}_2\text{O}_2\text{Se}$  is  $3.272 \text{ \AA}$ . As  $r_{\text{Bi-Se}} > r_{\text{Bi}^{3+}} + r_{\text{Se}^{2-}}$ , which indicates that Bi and Se are held by a weak electrostatic interaction.<sup>6</sup> This results in a small restoring force ( $F$ ). At the same time, the average mass ( $M$ ) is relatively large due to the large atomic mass of Bi atoms. Therefore, the low group velocity results from the weak bonding strength and heavy atomic mass. For comparison, the bond length of Bi-Se in  $\text{Bi}_2\text{Se}_3$  is  $2.891 \text{ \AA}$  and  $3.034 \text{ \AA}$ , smaller than that in  $\text{Bi}_2\text{O}_2\text{Se}$ .<sup>6</sup> This indicates that the existence of oxygen atoms further reduces the interaction between Bi and Se, hence leading to the lower thermal conductivity of  $\text{Bi}_2\text{O}_2\text{Se}$  than  $\text{Bi}_2\text{Se}_3$ .

In addition, lattice anharmonicity causes inherent scattering in materials, which reduces the relaxation time of phonons. The strong anharmonicity will significantly increase the scattering and lower the phonon relaxation time.<sup>18</sup> This generates a low thermal conductivity. The Gruneisen parameter ( $\gamma$ ), which reflects the degree of phonon vibration deviating from the harmonic oscillation in a lattice, is often referred to as an anharmonic parameter. The  $\gamma$  of  $\text{Bi}_2\text{O}_2\text{Se}$  can be calculated by the following equation:<sup>19</sup>

$$\gamma = \frac{3}{2} \left( \frac{1 + \nu_p}{2 - 3\nu_p} \right), \quad (4)$$

$\nu_p$  is the Poisson's ratio which has the following relationship with the longitudinal sound velocity ( $v_l$ ) and transverse sound velocity ( $v_s$ )<sup>19</sup>

$$\nu_p = \frac{1 - 2(v_s/v_l)^2}{2 - 2(v_s/v_l)^2}. \quad (5)$$

For bulk  $\text{Bi}_2\text{O}_2\text{Se}$ ,  $v_l$  is  $3541.6 \text{ m/s}$  and  $v_s$  is  $1637.4 \text{ m/s}$ .<sup>20</sup> The calculated value of  $\gamma$  is  $2.2$ , which is higher than those of the thermoelectric materials of  $\text{BiCuOSe}$  ( $1.5$ ) and  $\text{PbTe}$  ( $1.45$ ).<sup>19,21</sup> For  $\text{Bi}_2\text{Se}_3$ ,  $v_l$  is  $2900 \text{ m/s}$  and  $v_s$  is  $1700 \text{ m/s}$ .<sup>22</sup> The calculated  $\gamma$  of  $\text{Bi}_2\text{Se}_3$  is  $1.45$ . We have summarized the  $v_l$ ,  $v_s$ ,  $\gamma$  of these materials in Table S1. This indicates that the introduction of oxygen atoms greatly enhances the system's anharmonicity and results in the much lower thermal conductivity of  $\text{Bi}_2\text{O}_2\text{Se}$ . The strong anharmonicity of  $\text{Bi}_2\text{O}_2\text{Se}$  originates from the  $s^2$  lone pair electrons on group V atom, Bi.<sup>23</sup> Moreover, the weaker bonding strength in  $\text{Bi}_2\text{O}_2\text{Se}$  can be perceived as a stress buffer to dissipate lateral phonon transport.

The  $\kappa$  values of  $\text{Bi}_2\text{O}_2\text{Se}$  with different thicknesses are shown in Fig. 2(d). With the thickness decreasing from  $\sim 40$  to  $\sim 8$  nm,  $\kappa$  decreases from  $1.91 \pm 0.24$  to  $0.92 \pm 0.18 \text{ W}\cdot\text{m}^{-1}\cdot\text{K}^{-1}$ . The thickness

dependence of thermal conductivity in  $\text{Bi}_2\text{O}_2\text{Se}$  flakes is derived from the strong surface scattering of acoustic phonons.<sup>24</sup> (detailed analysis is given in the supplement.)

In addition to the in-plane thermal conductivity, the interfacial thermal conductance of 2D materials to the substrate is also the focus of attention.<sup>25</sup> Interfacial thermal conductance plays a key role as the main way of heat dissipation for electronic devices. For interfacial thermal conductance measurement, electric Joule heating replaces laser heating and Raman spectroscopy is used as a thermometer [Fig. 3(a)]. The laser power used is less than  $30 \mu\text{W}$ , which does not affect the operating temperature of the device. The inset of Fig. 3(b) depicts the optical image of a device with a typical field effect transistor (FET) configuration employed for measuring the interfacial thermal conductance of  $\text{Bi}_2\text{O}_2\text{Se}$ . The length and width of the device channel are  $3\text{--}5 \mu\text{m}$ . A good linear behavior is observed in the  $I_d - V_{ds}$  characteristics of  $\text{Bi}_2\text{O}_2\text{Se}$  flakes with different thicknesses, indicating Ohmic contacts between Au electrodes and  $\text{Bi}_2\text{O}_2\text{Se}$  [Fig. 3(b)]. As the electric power increases, the temperature of the device rises. It gives rise to the shift of the Raman peaks. As shown in Fig. S4(a), after applying a certain bias voltage, the characteristic Raman peaks of the  $\text{Bi}_2\text{O}_2\text{Se}$  channel show a significant red shift. When the same electrical power is applied, the temperature rise of the  $\text{Bi}_2\text{O}_2\text{Se}$  thin layer is lower than that of the thicker flakes [Fig. 3(c)], indicating better heat dissipation of the thinner  $\text{Bi}_2\text{O}_2\text{Se}$ .

To determine the interfacial thermal conductance between the  $\text{Bi}_2\text{O}_2\text{Se}$  and  $\text{SiO}_2/\text{Si}$  substrate, we consider the heat transfer from top to bottom as an equivalent thermal circuit<sup>25</sup>

$$\Delta T = P \times R_{tot}, \quad (6)$$

$$R_{tot} = R_{int} + R_{\text{SiO}_2} + R_{\text{SiO}_2,\text{Si}} + R_{\text{Si}}, \quad (7)$$

$$ITC = 1/R_{int}. \quad (8)$$

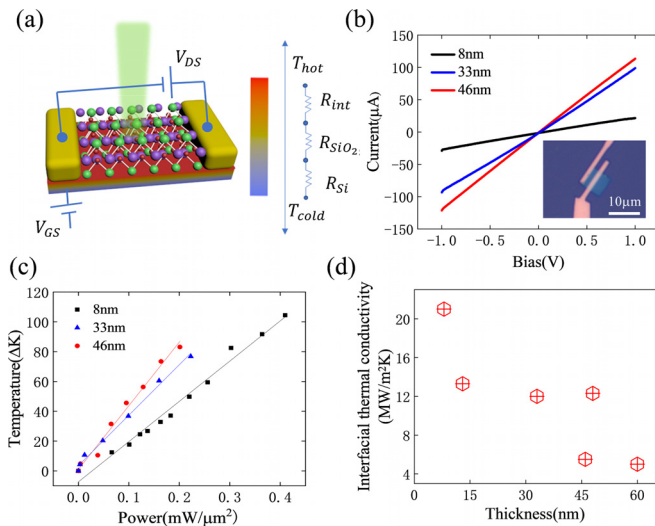


**FIG. 3.** Energy dissipation in the  $\text{Bi}_2\text{O}_2\text{Se}$  device. (a) Schematic illustration of the device and its equivalent thermal circuit. (b) Electrical transport characteristic of devices built on  $\text{Bi}_2\text{O}_2\text{Se}$  flakes with different thicknesses. (c) Temperature variations of  $\text{Bi}_2\text{O}_2\text{Se}$  flakes as a function of electrical power. (d) The thickness-dependent interfacial thermal conductance values of the  $\text{Bi}_2\text{O}_2\text{Se}$ - $\text{SiO}_2/\text{Si}$  system.

$R_{tot}$  is the total thermal resistance calculated from the slope of Fig. 3(c).  $R_{int}$  is the thermal resistance between  $\text{Bi}_2\text{O}_2\text{Se}$  and  $\text{SiO}_2/\text{Si}$ .  $R_{\text{SiO}_2} = t_{\text{SiO}_2}/\kappa_{\text{SiO}_2}$  is the thermal resistance of  $\text{SiO}_2$ , where  $t_{\text{SiO}_2} = 300 \text{ nm}$  and  $\kappa_{\text{SiO}_2} = 1.36 \text{ W}\cdot\text{m}^{-1}\cdot\text{K}^{-1}$  are the thickness and thermal conductivity of  $\text{SiO}_2$ , respectively. Since the thermal resistance between Si and  $\text{SiO}_2$  is extremely low ( $R \approx 10^{-9} \text{ m}^2\cdot\text{K}\cdot\text{W}^{-1}$ ),  $R_{\text{SiO}_2,\text{Si}}$  is negligible.  $R_{\text{Si}} \approx \sqrt{WL}/2\kappa_{\text{Si}}$  is the thermal resistance of Si, where  $W, L, \kappa_{\text{Si}} \approx 148 \text{ W}\cdot\text{m}^{-1}\cdot\text{K}^{-1}$  are the length and width of the channel, and the thermal conductivity of Si, respectively. The calculated interfacial thermal conductance of  $\text{Bi}_2\text{O}_2\text{Se}$  with different thicknesses is summarized in Fig. 3(d). The results show that the interfacial thermal conductance of the  $\text{Bi}_2\text{O}_2\text{Se}$  and substrate has a strong thickness dependence. The interfacial thermal conductance increases from  $\sim 5$  to  $\sim 21 \text{ MW}\cdot\text{m}^{-2}\cdot\text{K}^{-1}$  with the thickness decreasing from  $\sim 60 \text{ nm}$  to  $\sim 8 \text{ nm}$ . The thickness-dependent interfacial thermal conductance originates from the interfacial adhesion energy and the interfacial coupling strength of the  $\text{Bi}_2\text{O}_2\text{Se}/\text{SiO}_2$  system.

The interface adhesion energy determines the surface heat transfer performance.<sup>26</sup> For 2D materials, the strong thickness dependence of Young's modulus arises from the strain change caused by the large surface-volume-ratio, especially when the thickness is less than  $10 \text{ nm}$ .<sup>27,28</sup> As the thickness decreases, the increasing Young's modulus leads to the increase of interface adhesion.<sup>26</sup> The increased interface adhesion can enhance the strength of interlayer phonon-phonon coupling and raise the probability ( $\tau$ ) that phonons excited in  $\text{Bi}_2\text{O}_2\text{Se}$  impinge and transfer to the substrate. This facilitates the better breakdown (BD) characteristic of thinner  $\text{Bi}_2\text{O}_2\text{Se}$ . Figure S4(b) shows that the BD occurs near the drain electrode and the maximum BD power is  $\sim 0.89 \text{ mW}\cdot\mu\text{m}^{-2}$ .

In summary, we systematically investigated the lateral thermal transport and energy dissipation in  $\text{Bi}_2\text{O}_2\text{Se}$  thin flakes. We find that the in-plane thermal conductivity of  $\text{Bi}_2\text{O}_2\text{Se}$  decreases with reducing thickness. A low thermal conductivity of  $0.92 \pm 0.18 \text{ W}\cdot\text{m}^{-1}\cdot\text{K}^{-1}$  is shown by the  $\text{Bi}_2\text{O}_2\text{Se}$  thin layer with a thickness of  $\sim 8 \text{ nm}$ . This renders great potential for thermoelectric application. The low thermal conductivity results from a low phonon group velocity, strong anharmonicity, and large surface phonon dispersion in the 2D  $\text{Bi}_2\text{O}_2\text{Se}$  thin layer. The operating temperature as a function of electric power in the  $\text{Bi}_2\text{O}_2\text{Se}$  device was also investigated. Different from the in-plane thermal conductivity, the interfacial thermal conductance between  $\text{Bi}_2\text{O}_2\text{Se}$  and  $\text{SiO}_2/\text{Si}$  increases with decreasing thickness. Because of the larger interface adhesion energy,  $\text{Bi}_2\text{O}_2\text{Se}$  thin layers show better heat dissipation than their thick counterparts. These results provide critical information for the design of the  $\text{Bi}_2\text{O}_2\text{Se}$ -based high figure of merit thermoelectric and low-power electronics devices.

See the [supplementary material](#) for the detailed optical images, AFM data, EDX data, SEM, spot size, optical absorption coefficients, and Raman frequency evolution.

Z.N. and J.L. thank the support of the National Key Research and Development Program of China (No. 2017YFA0205700), the NSFC (Nos. 11704068 and 61774034), the Jiangsu Natural Science Foundation (No. BK20170694), the Strategic Priority Research Program of the Chinese Academy of Sciences (No. XDB30000000), and the Fundamental Research Funds for the Central Universities.

## REFERENCES

- <sup>1</sup>A. A. Balandin, S. Ghosh, W. Bao, I. Calizo, D. Teweldebrhan, F. Miao, and C. N. Lau, *Nano Lett.* **8**, 902 (2008).
- <sup>2</sup>A. A. Balandin, *Nat. Mater.* **10**, 569 (2011).
- <sup>3</sup>S. Lin, W. Li, S. Li, X. Zhang, Z. Chen, Y. Xu, and Y. Pei, *Joule* **1**, 816 (2017).
- <sup>4</sup>S. S. Naghavi, J. He, Y. Xia, and C. Wolverton, *Chem. Mater.* **30**, 5639 (2018).
- <sup>5</sup>M. Samanta, K. Pal, P. Pal, U. V. Waghmare, and K. Biswas, *J. Am. Chem. Soc.* **140**, 5866 (2018).
- <sup>6</sup>J. Wu, H. Yuan, M. Meng, C. Chen, Y. Sun, Z. Chen, and Y. Zhou, *Nat. Nanotechnol.* **12**, 530 (2017).
- <sup>7</sup>S. Sahoo, A. P. Gaur, M. Ahmadi, M. J. F. Guinel, and R. S. Katiyar, *J. Phys. Chem. C* **117**, 9042 (2013).
- <sup>8</sup>Y. Zhao, G. Zhang, M. H. Nai, G. Ding, D. Li, Y. Liu, and J. Wu, *Adv. Mater.* **30**, 1804928 (2018).
- <sup>9</sup>J. Yu and Q. SunYu, *J. Appl. Phys. Lett.* **112**, 053901 (2018).
- <sup>10</sup>P. Ruleva, C. Drasar, and P. Lostak, *Mater. Chem. Phys.* **119**, 299–302 (2010).
- <sup>11</sup>C. Drasar, P. Ruleova, L. Benes, and P. Lostak, *J. Electron. Mater.* **41**, 2317–2321 (2012).
- <sup>12</sup>T. Cheng, C. Tan, S. Zhang, T. Tu, H. Peng, and Z. Liu, *J. Phys. Chem. C* **122**, 19970 (2018).
- <sup>13</sup>N. Peimyoo, J. Shang, W. Yang, Y. Wang, C. Cong, and T. Yu, *Nano Res.* **8**, 1210 (2015).
- <sup>14</sup>A. N. Lanzillo, A. Glen Birdwell, M. Amani, F. J. Crowne, P. B. Shah, S. Najmaei, and S. K. Nayak, *Appl. Phys. Lett.* **103**, 093102 (2013).
- <sup>15</sup>T. Wang, M. Han, R. Wang, P. Yuan, S. Xu, and X. Wang, *J. Appl. Phys.* **123**, 145104 (2018).
- <sup>16</sup>Y. Zhang, T. Day, M. L. Snedaker, C. S. Birkel, and G. D. Stucky, *Adv. Mater.* **24**, 5065 (2012).
- <sup>17</sup>Z. Chen, X. Zhang, and Y. Pei, *Adv. Mater.* **30**, 1705617 (2018).
- <sup>18</sup>J. P. Heremans, *Nat. Phys.* **11**, 990 (2015).
- <sup>19</sup>Y. L. Pei, F. Li, Q. Liu, W. Pan, and L. D. Zhao, *NPG Asia Mater.* **5**, e47 (2013).
- <sup>20</sup>X. Tan, Y. Liu, and K. Hu, *J. Am. Ceram. Soc.* **101**, 326 (2018).
- <sup>21</sup>M. Roufosse and P. G. Klemens, *Phys. Rev. B* **7**, 5379 (1973).
- <sup>22</sup>Y. D. Glinka, S. Babakiray, and T. A. Johnson, *J. Appl. Phys.* **117**, 165703 (2015).
- <sup>23</sup>D. M. Nielsen, V. Ozolins, and P. J. Heremans, *Energy Environ. Sci.* **6**, 570–578 (2013).
- <sup>24</sup>Z. Luo, J. Maassen, Y. Deng, Y. Du, R. P. Garrelts, M. S. Lundstrom, and X. Xu, *Nat. Commun.* **6**, 8572 (2015).
- <sup>25</sup>C. J. Foss and Z. Aksamija, *2D Mater.* **6**, 025019 (2019).
- <sup>26</sup>L. Zhang and G. Ouyang, *J. Phys. D: Appl. Phys.* **52**, 025302 (2019).
- <sup>27</sup>C. Li, Y. Bando, C. Zhi, Y. Huang, and D. Golberg, *Nanotechnology* **20**, 385707 (2009).
- <sup>28</sup>Y. He, W. F. Chen, W. B. Yu, G. Ouyang, and G. W. Yang, *Sci. Rep.* **3**, 2660 (2013).